

A theory for formation of a low pressure, current-free double layer

M A Lieberman¹, C Charles and R W Boswell

Space Plasma, Power and Propulsion, Research School of Physical Sciences and Engineering, Australian National University, ACT 0200, Australia

Received 29 March 2006, in final form 7 June 2006

Published 21 July 2006

Online at stacks.iop.org/JPhysD/39/3294

Abstract

A theory is developed for the formation of a low pressure, current-free double layer just inside an upstream dielectric source chamber connected to a larger diameter, downstream metallic expansion chamber. The double layer is described using four groups of charged particle: thermal ions, mono-energetic accelerated ions flowing downstream, accelerated electrons flowing upstream and thermal electrons. The accelerated electrons are formed downstream from an initially nearly half-Maxwellian electron distribution. A fifth group of counter-streaming electrons formed by the reflection of the accelerated electrons from the sheath at the insulated end wall of the source chamber is used to enforce the condition that the double layer be current-free. The condition of particle balance upstream is found to determine the double layer potential. The double layer is found to disappear at very low pressures due to loss of ionization balance upstream and due to energy relaxation processes for ionizing electrons at higher pressures. The theory is found to be in good agreement with the experiments.

(Some figures in this article are in colour only in the electronic version)

1. Introduction

Although double layers have been studied for decades, most theoretical papers have dealt with current-driven double layers [1]. There has been considerable interest in the formation of current-free double layers in low pressure rf-driven plasmas [2–4] and in their application to such diverse fields as plasma thrusters for space propulsion [2, 5] and the physics of the solar corona [5, 6]. In one recent experiment [2, 7], shown schematically in figure 1, a plasma created by the 13.56 MHz excitation of a helicon-type antenna wrapped around a cylindrical insulating source chamber is connected to a larger diameter metallic expansion chamber. The parameters are source length and radius $h = 31$ cm and $R_2 = 6.85$ cm and expansion chamber length and radius $w = 29.4$ cm and $R_1 = 15.9$ cm. At argon pressures in the range 0.2–2 mTorr, ion energy analyzer measurements show that a thin double layer is formed in the source chamber a short distance from its junction with the expansion chamber. The voltage across the double layer is measured to be as high as ~ 25 V at the lowest

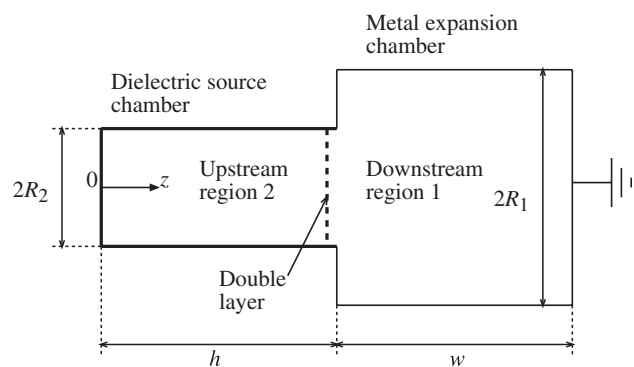


Figure 1. Schematic diagram of double layer formation at the junction between a small diameter upstream source plasma and a larger diameter downstream expansion plasma.

pressure (0.2 mTorr). For pressures below 0.2 mTorr or above 2 mTorr, the double layer disappears.

In this work, we develop a theory that couples the dynamics of the particles in the non-neutral double layer to the diffusive flows of the quasi-neutral plasmas in the source

¹ Permanent address: Department of Electrical Engineering and Computer Science – 1770, University of California, Berkeley, CA 94720, USA.

and expansion chambers. The theory is found to be in good agreement with the experiments.

Langmuir [8] first described a double layer formed between an electron-emitting cathode and an ion-emitting anode, with an applied dc voltage across the gap. The space charge density is negative near the cathode and positive near the anode. Langmuir showed that the sum of positive and negative charge within the gap vanishes when

$$I_e = (M/m)^{1/2} I_i, \quad (1)$$

where I_e and I_i are the electron and ion currents flowing across the gap and m and M are the electron and ion masses.

Andrews and Allen [9] obtained conditions to embed a double layer in a quasi-neutral plasma using four groups of charged particles inside the double layer: (a) thermal ions, (b) accelerated ions flowing downstream, (c) accelerated electrons flowing upstream and (d) thermal electrons. For assumed mono-energetic accelerated species and Maxwellian thermal species, Andrews and Allen determined the density ratios of the species at each edge of the double layer, as well as the entering velocities required for the accelerated species, at a given double layer potential drop. In section 2, we introduce an initially near-half-Maxwellian, rather than mono-energetic, accelerated electron group, to more realistically describe the experiments. To treat the formation of a current-free double layer, as seen in the experiments, we assume that the accelerated electrons are (almost entirely) reflected from the end wall of the source region, forming a counter-streaming population.

In section 3, the densities and particle fluxes at each edge of the double layer are coupled to the particle balance relations upstream and downstream, using low pressure diffusion theory. At low pressures, the upstream and downstream thermal ionization rates are equal, but the particle loss rate is greater upstream than downstream, due to the smaller upstream radius. The accelerated electron group supplies the additional ionization rate required upstream. The ionization rate for this group depends on, and thus determines, the double layer potential. A high pressure limit is determined for the double layer formation, when the energy relaxation length for ionizing electrons (~ 20 V) becomes important compared with the system length. Comparisons of the theory with the experiments are given in section 4. We also give a discussion of some additional theoretical and experimental issues, in this section.

2. Double layer formation

We follow the procedure and notation of [9], with subscripts a , b , c and d referring to thermal ions, accelerated ions, accelerated electrons and thermal electrons, respectively, and subscripts 1 and 2 referring to the downstream and upstream double layer edges, respectively. Choosing the zero of potential at the downstream edge, with a potential V_s at the upstream edge, the charge density within the double layer is determined by solving Poisson's equation for the potential V . For the thermal ions and electrons, the charge densities are given by the corresponding Boltzmann relations

$$\rho_a = \rho_{a1} e^{-V/T_i}, \quad (2)$$

$$\rho_d = \rho_{d2} e^{-(V_s - V)/T_e}, \quad (3)$$

where ρ_{a1} and ρ_{d2} are the thermal ion and electron densities at the downstream and upstream edge, respectively. In (2) and (3), and throughout this work, the symbols $T_i = kT_{ik}/e$ and $T_e = kT_{ek}/e$ are the ion and electron temperatures in equivalent-voltage units (volts), where $k = 1.38 \times 10^{-23} \text{ J K}^{-1}$ is Boltzmann's constant, $e = 1.6 \times 10^{-19} \text{ C}$ is the unit of charge and T_{ik} and T_{ek} are the ion and electron temperatures in kelvins. For mono-energetic ions entering the double layer upstream with velocity v_i and charge density ρ_{b2} , the charge density is determined by particle flux and energy conservation within the double layer

$$\rho_b v_z = \rho_{b2} v_i; \quad v_z^2 = v_i^2 + 2e(V_s - V)/M, \quad (4)$$

which yields

$$\rho_b = \rho_{b2} [1 + 2e(V_s - V)/Mv_i^2]^{-1/2}. \quad (5)$$

In appendix A, we treat mono-energetic accelerating electrons flowing upstream, first described in [9]. Here, we introduce a nearly-half-Maxwellian energy distribution, which more realistically describes the energy distribution seen in the experiments. At the low pressures of the experiments, the energy relaxation length for electrons with energies below the first excitation potential of argon (~ 11.6 V) is much larger than the system length. Therefore, we choose the same characteristic T_e for the accelerated group (c) as for the trapped electron group (d). As discussed in [9], the distribution function must be zero at $v_z = 0$. We therefore introduce a near-half-Maxwellian electron distribution

$$f_{c1} = \frac{2n_{c1}}{\text{erfc}(\zeta_1)} \left(\frac{m}{2\pi e T_e} \right)^{1/2} e^{-mv_z^2/2eT_e} \quad v_z > v_e \quad (6)$$

$$= 0 \quad v_z < v_e$$

where $\zeta_1 = (mv_e^2/2eT_e)^{1/2}$, $n_{c1} = -\rho_{c1}/e$, erfc is the complementary error function and the normalization is $\int f_{c1} dv_z = n_{c1}$. The velocity v_e will be shown to be of order $(eT_i/m)^{1/2}$, which is much smaller than the electron thermal velocity for $T_i \ll T_e$. The corresponding charge density is

$$\rho_c = -e \int_{v_e}^{\infty} v_z (v_z^2 + 2eV/m)^{-1/2} f_{c1} dv_z. \quad (7)$$

Evaluating the integral yields

$$\rho_c = \rho_{c1} \frac{\text{erfc}(\zeta)}{\text{erfc}(\zeta_1)} e^{-V/T_e} \quad (8)$$

with $\zeta = [(mv_e^2 + 2eV)/2eT_e]^{1/2}$.

We introduce [9] the normalized quantities $\tau_e = T_e/V_s$, $\tau_i = T_i/V_s$, $\eta = V/V_s$, $\Phi_e = mv_e^2/2eV_s$ and $\Phi_i = Mv_i^2/2eV_s$ such that $\zeta_1 = (\Phi_e/\tau_e)^{1/2}$ and $\zeta = [(\Phi_e + \eta)/\tau_e]^{1/2}$. The total charge density is $\rho(\eta) = \rho_a + \rho_b + \rho_c + \rho_d$.

The boundary conditions at the downstream and upstream edges are

$$\rho = 0 \quad \text{at } \eta = 0; \quad \rho = 0 \quad \text{at } \eta = 1, \quad (9)$$

$$d\rho/d\eta = 0 \quad \text{at } \eta = 0; \quad d\rho/d\eta = 0 \quad \text{at } \eta = 1. \quad (10)$$

Boundary conditions (10) are discussed in [9]; they are equivalent to the Bohm condition [10] for a collisionless

plasma joining a collisionless sheath, such that the space derivatives of the total electron and ion densities at the sheath edge must be equal.

The four equations (9) and (10) have the form

$$\begin{bmatrix} g_{11} & g_{12} & g_{13} & g_{14} \\ g_{21} & g_{22} & g_{23} & g_{24} \\ g_{31} & g_{32} & g_{33} & g_{34} \\ g_{41} & g_{42} & g_{43} & g_{44} \end{bmatrix} \begin{bmatrix} \rho_{a1} \\ \rho_{b2} \\ \rho_{c1} \\ \rho_{d2} \end{bmatrix} = 0 \quad (11)$$

with the coefficients

$$\begin{aligned} g_{11} &= 1; & g_{12} &= (1 + \Phi_i^{-1})^{-1/2}; & g_{13} &= 1; & g_{14} &= e^{-1/\tau_e}; \\ g_{21} &= e^{-1/\tau_i}; & g_{22} &= 1; & g_{23} &= e^{1/\tau_e} \operatorname{erfc}(\zeta_2) / \operatorname{erfc}(\zeta_1); \\ g_{24} &= 1; & g_{31} &= -1/\tau_i; & g_{32} &= \frac{1}{2} \Phi_i^{-1} (1 + \Phi_i^{-1})^{-3/2}; \\ g_{33} &= \tau_e^{-1} [1 - e^{-\zeta_1^2} / \sqrt{\pi} \zeta_1 \operatorname{erfc}(\zeta_1)]; & g_{34} &= \tau_e^{-1} e^{-1/\tau_e}; \\ g_{41} &= -\tau_i^{-1} e^{-1/\tau_i}; & g_{42} &= \frac{1}{2} \Phi_i^{-1}; \\ g_{43} &= \tau_e^{-1} [e^{1/\tau_e} \operatorname{erfc}(\zeta_2) - e^{-\zeta_1^2} / (\sqrt{\pi} \zeta_2)] / \operatorname{erfc}(\zeta_1); \\ g_{44} &= 1/\tau_e \end{aligned} \quad (12)$$

with $\zeta_2 = [(\Phi_e + 1)/\tau_e]^{1/2}$. The determinant of the coefficient matrix must vanish for a non-zero solution of (11)

$$\det[\mathbf{g}] = 0. \quad (13)$$

The ratios of the charge densities are then given by the ratios of the cofactors of the first row of $[\mathbf{g}]$

$$\rho_{a1} : \rho_{b2} : \rho_{c1} : \rho_{d2} :: C_{11} : C_{12} : C_{13} : C_{14}. \quad (14)$$

The final condition required to determine the double layer parameters is that the sum of positive and negative charge in the double layer must vanish or, equivalently, that the total force acting on the double layer must vanish:

$$\int_0^1 \rho(\eta) d\eta = 0. \quad (15)$$

Condition (15) ensures that a zero electric field at one edge of the double layer leads to a zero electric field at the opposite edge. Evaluating (15), we obtain

$$E_1 \rho_{a1} + E_2 \rho_{b2} + E_3 \rho_{c1} + E_4 \rho_{d2} = 0, \quad (16)$$

where

$$\begin{aligned} E_1 &= \tau_i (1 - e^{-1/\tau_i}), & E_2 &= 2\Phi_i [(1 + \Phi_i^{-1})^{1/2} - 1], \\ E_3 &= \tau_e [2(\zeta_2 - \zeta_1) e^{-\zeta_1^2} / \sqrt{\pi} \operatorname{erfc}(\zeta_1) \\ &\quad + e^{1/\tau_e} \operatorname{erfc}(\zeta_2) / \operatorname{erfc}(\zeta_1) - 1], \\ E_4 &= \tau_e (1 - e^{-1/\tau_e}). \end{aligned} \quad (17)$$

Substituting (14) into (16) yields

$$C_{11} E_1 + C_{12} E_2 + C_{13} E_3 + C_{14} E_4 = 0. \quad (18)$$

For given values τ_i and τ_e , the simultaneous solution of (13) and (18) determines Φ_i and Φ_e . Once these are found, then

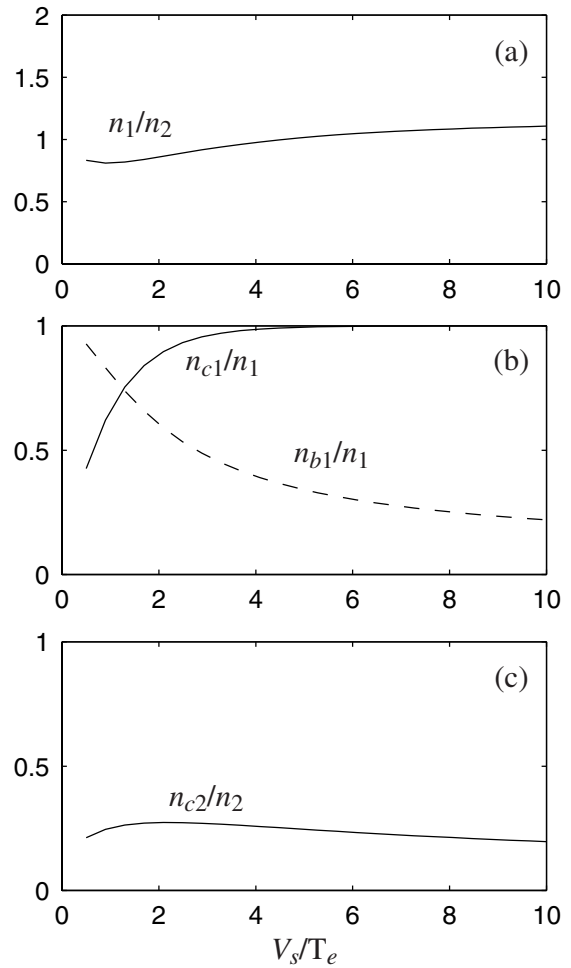


Figure 2. Density ratio versus double layer strength V_s/T_e ; (a) n_1/n_2 ; (b) n_{c1}/n_1 (—) and n_{b1}/n_1 (---) and (c) n_{c2}/n_2 .

the densities are obtained from (14). Except for a common constant of proportionality, these are

$$\begin{aligned} n_{a1} &= C_{11}/e; & n_{a2} &= g_{21} C_{11}/e; & n_{b1} &= g_{12} C_{12}/e; \\ n_{b2} &= C_{12}/e; & n_{c1} &= -C_{13}/e; & n_{c2} &= -g_{23} C_{13}/e; \\ n_{d1} &= -g_{14} C_{14}/e; & n_{d2} &= -C_{14}/e. \end{aligned} \quad (19)$$

Equations (13) and (18) are highly nonlinear and must be solved numerically. We have obtained the solutions and verified their relative accuracy to within 0.1%. Figure 2(a) shows the ratio of total downstream-to-upstream density n_1/n_2 as a function of the double layer strength V_s/T_e , for an assumed ion-to-electron temperature ratio $T_i/T_e = 0.05$. Here $n_1 = n_{a1} + n_{b1}$ and $n_2 = n_{a2} + n_{b2}$. The density ratio is nearly unity over the entire range of strengths. Figure 2(b) gives the densities for the accelerated electron group (solid line) and the accelerated ion group (dashed line) as fractions of the total downstream density. The electron group rises sharply to 100% of the total as V_s/T_e increases, and the ion group falls from nearly 100% to 20% over the range of V_s/T_e shown. The electron group is about 90% of the total downstream density and the ion group is about 55%, for $V_s/T_e = 2$. Figure 2(c) gives the density of the accelerated electron group as a fraction of the total upstream density. The

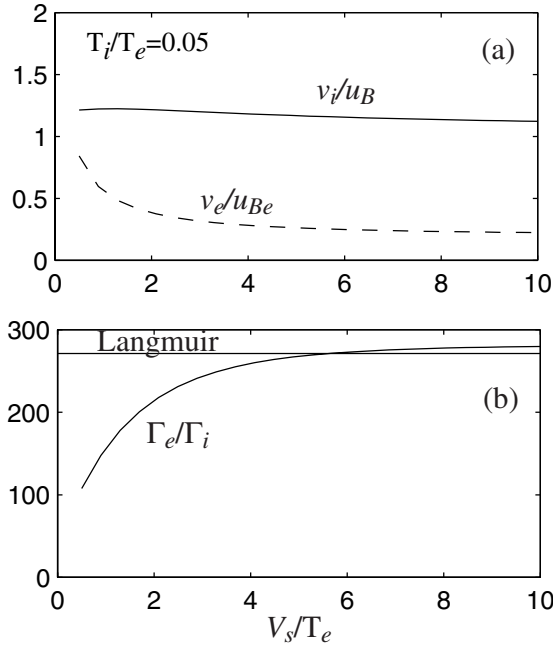


Figure 3. (a) Ion velocity v_i (—) and electron velocity v_e (---) entering the double layer versus V_s/T_e ; the ion velocity is normalized to $u_B = (eT_e/M)^{1/2}$ and the electron velocity to $u_{Be} = (eT_i/m)^{1/2}$; (b) the ratio of electron-to-ion flux for the accelerated species versus V_s/T_e ; the Langmuir condition (1) is shown as the solid horizontal line.

accelerated electrons comprise about 20% of the upstream density, relatively independent of the ratio V_s/T_e . There is a negligible thermal ion density n_{a2} passing from downstream to upstream. Figure 3(a) gives the ratios v_i/u_B (solid line) and v_e/u_{Be} (dashed line), where $u_B = (eT_e/M)^{1/2}$ is the usual Bohm velocity and $u_{Be} = (eT_i/m)^{1/2}$ is a similar velocity defined for electrons. The accelerating ion group is seen to enter the double layer at a velocity of 1.2–1.3 u_B . The entering velocity v_e for the lowest energy electrons in the accelerating electron distribution is seen to be in the range 0.2–1 u_{Be} , which is small compared with $(eT_e/m)^{1/2}$. These results are found to be practically independent of T_i/T_e over the range 0.01–0.06, except that v_e decreases as T_i/T_e decreases. The ratio of electron-to-ion flux for the accelerating species

$$\Gamma_e/\Gamma_i = \frac{n_{c1} u_B}{n_{b2} v_i} \frac{e^{-\zeta_1^2}}{\text{erfc}(\zeta_1)} \left(\frac{2M}{\pi m} \right)^{1/2} \quad (20)$$

is compared with the Langmuir ratio (1) in figure 3(b). At low double layer strengths, we see a significant reduction compared with the Langmuir ratio.

The entire source chamber is insulating in the experiments, such that the net (electrical) current flowing into the source must vanish. To apply the preceding results to this situation, a fifth species is introduced, which is formed by the reflection of (almost) all the accelerated electron group by the sheath at the upstream wall. It is easily seen that this reflected group contributes exactly the same charge density to the double layer and to the downstream plasma as the original group. Hence, the double layer solution is unaltered by the addition of the reflected electron group. In this sense, there is no fundamental distinction between a current-carrying and a

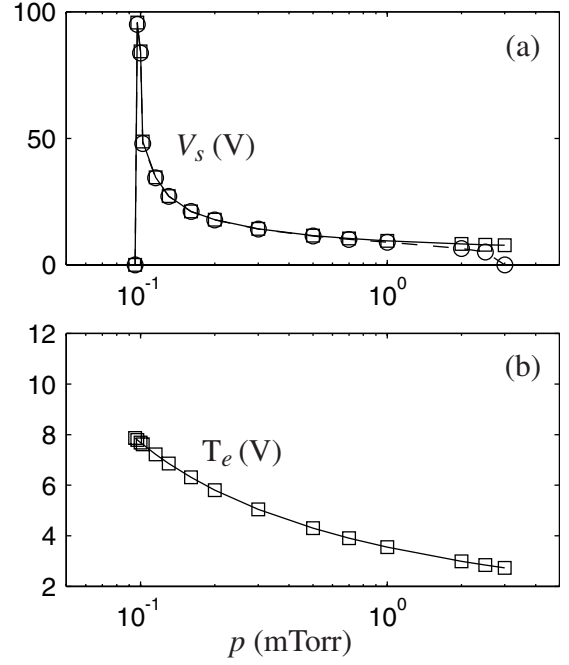


Figure 4. (a) Double layer strength V_s versus pressure p without (\square) and with (\circ) accounting for the energy relaxation length of ionizing electrons; (b) electron temperature T_e versus pressure p ; the lines are drawn to guide the eye.

current-free double layer [11]. The slight imbalance in currents between the incident and reflected accelerated and thermal electron groups balances the flow of ions to the upstream wall. The resulting floating potential that forms at the wall will be determined in section 3.

3. Downstream and upstream particle balance

The downstream particle balance is determined by low pressure diffusion theory [12, section 10.2] according to the relation

$$K_{iz} n_g \pi R_1^2 \cdot 2w = (2\pi R_1^2 h_{2w} + 2\pi R_1 \cdot 2wh_{R_1}) u_B, \quad (21)$$

where $K_{iz}(T_e)$ is the ionization rate coefficient for thermal (Maxwellian) electrons, n_g is the neutral gas density,

$$h_{2w} = 0.86 (3 + w/\lambda_i)^{-1/2}, \quad h_{R_1} = 0.8 (4 + R_1/\lambda_i)^{-1/2} \quad (22)$$

are the axial and radial edge-to-centre density ratios, given from low pressure diffusion theory [12, p 148] and $\lambda_i \approx (330 p)^{-1}$ is the thermal ion mean free path in argon, with λ_i in cm and p in Torr. Solving (21) determines T_e in the entire system at any given pressure. Guided by the experiments and the results from the double layer theory, we have assumed in (21) and (22) that the thermal ion diffusion flux flowing upstream into the source chamber is negligible.

Because the upstream radius is smaller than the downstream radius, ionization by thermal electrons upstream does not suffice to balance the larger particle losses upstream at low pressures. An additional source of upstream ionization is required, which is supplied by the accelerated group of electrons. We use a simplified one-dimensional diffusion model for the particle balance upstream. Letting n_i ,

$n_d = n_i - n_{c2}$ and n_{c2} be the densities of ions, thermal electrons and accelerated electrons, with the latter species assumed to be uniform in z , then the diffusion equation is

$$-D_{A2} \frac{d^2 n_i}{dz^2} + v_R n_i = n_g (K_{iz} n_d + K_{izc} n_{c2}), \quad (23)$$

where

$$D_{A2} = h_{R2} u_B R_2 \quad (24)$$

is the low pressure ambipolar diffusion coefficient (see [appendix B](#)),

$$v_R = 2h_{R2} u_B / R_2 \quad (25)$$

is the radial loss frequency and K_{izc} is the ionization rate coefficient for the accelerated electron group. K_{izc} is a function of V_s and T_e and is calculated in [appendix C](#). We assume a symmetric solution for the ion density about $z = h/2$

$$n_i = \beta n_{c2} - n_{i0} \cosh \gamma \left(z - \frac{1}{2} h \right), \quad (26)$$

where

$$\beta = \frac{n_g (K_{izc} - K_{iz})}{(v_R - K_{iz} n_g)} \quad (27)$$

and

$$\gamma^2 = (v_R - K_{iz} n_g) / D_{A2} \quad (28)$$

is the square of the axial decay constant. The ion flux is

$$\Gamma_i = \gamma D_{A2} n_{i0} \sinh \gamma \left(z - \frac{1}{2} h \right). \quad (29)$$

Setting $\Gamma_i = n_i v_i$ at $z = h$ determines n_{i0} . The complete solution is then

$$n_i = \left[1 - \frac{\cosh \gamma \left(z - \frac{1}{2} h \right)}{(\gamma D_{A2} / v_i) \sinh \frac{1}{2} \gamma h + \cosh \frac{1}{2} \gamma h} \right] \beta n_{c2}. \quad (30)$$

Evaluating (30) at the upstream edge of the double layer $z = h$ yields

$$\beta = \left(1 + \frac{v_i}{\gamma D_{A2}} \coth \frac{1}{2} \gamma h \right) \frac{n_{i2}}{n_{c2}}, \quad (31)$$

where $n_{i2} = n_{a2} + n_{b2}$ is the total ion density at the upstream edge. The ratio n_{i2}/n_{c2} in (31) is given from (19). Equating (27) to (31) yields

$$\frac{n_g (K_{izc} - K_{iz})}{(v_R - K_{iz} n_g)} = \left(1 + \frac{v_i}{\gamma D_{A2}} \coth \frac{1}{2} \gamma h \right) \frac{n_{i2}}{n_{c2}}. \quad (32)$$

Since K_{izc} and n_{i2}/n_{c2} depend on V_s , (32) determines the double layer strength V_s needed for particle balance upstream.

Equation (32) has been solved numerically, and the results for V_s versus pressure p are given as the squares in figure 4, along with T_e determined by solving (21). We see that V_s rises dramatically as the pressure is decreased, with a minimum pressure of approximately 0.096 mTorr for a solution to exist. Below that pressure, the maximum ionization rate coefficient of $\sim 2.2 \times 10^{-13} \text{ m}^3 \text{ s}^{-1}$ for the accelerated electrons upstream (see figure C1) is not sufficient to balance the excess upstream particle losses. The maximum double layer strength is seen to be of the order 100 V near the minimum pressure but is a very sensitive function of pressure for such high values of V_s . Figure 5 shows the various density ratios corresponding

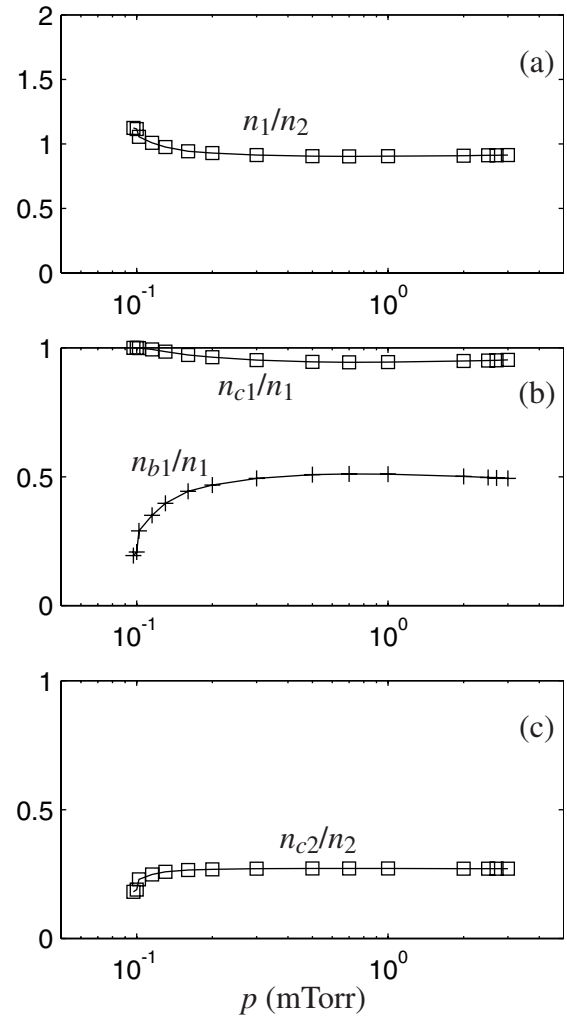


Figure 5. (a) Downstream-to-upstream density ratio n_1/n_2 , (b) downstream ratios n_{c1}/n_1 and n_{b1}/n_1 and (c) upstream ratio n_{c2}/n_2 versus pressure p for the solution shown in figure 4; the lines are drawn to guide the eye.

to figure 4. These have little variations with pressure except at the lowest pressures.

In the experiment, the double layer also disappears at pressures above a few milliTorr. To understand this, we examine the energy relaxation length for ionizing electrons [12, p 691],

$$\lambda_{iz} = (\lambda_{el} \lambda_{inel} / 3)^{1/2}, \quad (33)$$

where λ_{el} and λ_{inel} are the elastic and inelastic mean free paths for electrons in argon. For a 20 V electron, we find that $\lambda_{iz} \approx 30 \text{ cm}$ at 1 mTorr, which is comparable to the system length. Since electrons are heated upstream, the downstream ionizing electron density can be depleted at the higher pressures. When the ratio of downstream-to-upstream ionization rates becomes equal to the ratio of downstream-to-upstream particle loss rates, then the additional ionization provided by electrons accelerated upstream by the double layer is no longer needed. For a uniform ionizing density n_{iz2} upstream, the downstream density is

$$n_{iz1} = n_{iz2} \cosh[(h+w-z)/\lambda_{iz}] / \cosh(w/\lambda_{iz}); \quad h < z < h+w, \quad (34)$$

where we have assumed electron reflection from the downstream sheath. The average downstream density is

$$\bar{n}_{iz1} = \frac{1}{w} \int_h^{h+w} dz n_{iz1} = n_{iz2} \frac{\lambda_{iz}}{w} \tanh \frac{w}{\lambda_{iz}}. \quad (35)$$

Hence, for a given downstream ionization rate coefficient K_{iz} , the effective ionization rate coefficient upstream is larger and is given by

$$K_{izeff} = K_{iz} \frac{w}{\lambda_{iz}} \coth \frac{w}{\lambda_{iz}}. \quad (36)$$

Using (36) in place of K_{iz} in (32), we can solve to determine V_s , as previously. The results are shown in figure 4 as circles. We find that the double layer disappears at pressures above about 2.5 mTorr, as is seen experimentally.

Downstream, the accelerated ions enter the expansion chamber, where they undergo charge transfer collisions with the neutral gas, leading to the production of thermal ions. The experiments show that the characteristic radius of the beam ions inside the expansion chamber is that of the source chamber. The neutralizing electrons associated with the downstream beam ions also lead to additional ionization. A simplified diffusion model is used to describe these processes, in which the ionization and the volume rate of production of thermal ions due to the presence of the beam ions is assumed to be uniform within the expansion chamber. The downstream beam ion density is

$$n_b = n_{b1} e^{-(z-h)/\lambda_b}, \quad h < z < h+w; \quad r < R_2, \quad (37)$$

where $\lambda_b \approx 0.7\lambda_i$ is the beam ion–neutral charge transfer mean free path. The net number of beam ions per second converted to thermal ions in the expansion chamber is thus

$$n_{b1} v_b (1 - e^{-w/\lambda_b}) \pi R_2^2, \quad (38)$$

where $v_b = (v_i^2 + 2eV_s/M)^{1/2}$ is the beam ion velocity in the expansion chamber. Dividing by the volume of the expansion chamber, the volume rate of production of thermal ions is then $v_b n_{beff}$, where $v_b = v_b/\lambda_b$ is the charge transfer frequency and

$$n_{beff} = n_{b1} \frac{\lambda_b}{w} \frac{R_2^2}{R_1^2} (1 - e^{-w/\lambda_b}). \quad (39)$$

The diffusion equation for thermal ions downstream is

$$-D_{A1} \frac{d^2 n_i}{dz^2} + \nu_{R1} n_i = n_g K_{iz} (n_i + n_{beff}) + \nu_b n_{beff}, \quad (40)$$

where $D_{A1} = h_{R1} u_B R_1$ (see appendix B) and $\nu_{R1} = 2h_{R1} u_B / R_1$ is the downstream radial loss frequency. The solution is

$$n_i = n_{a1} \cos k_1 (z - h) + \alpha n_{beff} [\cos k_1 (z - h) - 1], \quad (41)$$

where

$$k_1^2 = (n_g K_{iz} - \nu_{R1}) / D_{A1} \quad (42)$$

is the square of the downstream axial wavenumber and

$$\alpha = \frac{k_1^2 D_{A1} + \nu_{R1} + \nu_b}{k_1^2 D_{A1}}. \quad (43)$$

The thermal ion flux is

$$\Gamma_i = k_1 D_{A1} (n_{a1} + \alpha n_{beff}) \sin k_1 (z - h). \quad (44)$$

Setting $\Gamma_i = n_i u_B$ at $z = h + w$ yields

$$k_1 D_{A1} (n_{a1} + \alpha n_{beff}) \sin k_1 w = u_B (n_{a1} + \alpha n_{beff}) \cos k_1 w - u_B \alpha n_{beff}. \quad (45)$$

Solving (45) for k_1 , we obtain the density profile from (40); k_1 is found to be real at low pressures and imaginary at higher pressures.

The potential distribution in the discharge is determined from the density distribution. With the zero of potential at the downstream wall and a floating potential of $V_{f1} = \frac{1}{2} T_e \ln(M/2\pi m) = 4.8 T_e$ across the sheath there, the downstream potential is

$$V_1(z) = 4.8 T_e + T_e \ln(n_e(z)/n_e(h+w)). \quad (46)$$

The upstream potential is

$$V_2(z) = V_1(h) + V_s + T_e \ln(n_{d2}(z)/n_{d2}(h)). \quad (47)$$

The potential drop V_{f2} across the sheath at the upstream floating wall is obtained by equating the ion and electron fluxes there

$$n_{i2} v_i = \frac{1}{4} \left(\frac{8eT_e}{\pi m} \right)^{1/2} (n_{d2} + n_{c1} e^{V_s/T_e}) e^{-V_{f2}/T_e}. \quad (48)$$

Figure 6 shows the density and potential profiles at low (0.1 mTorr), medium (0.3 mTorr) and high (1 mTorr) pressures. The potentials (with respect to earth) at the upstream and downstream walls are indicated by crosses. At low pressures, a large double layer potential drop V_s is seen, and the charge transfer of the ion beam with the neutrals is small. The medium and high pressure cases are similar, with a lower double layer potential and almost complete charge transfer of the ion beam.

4. Comparison of theory with measurements

In a relatively complete experiment in argon gas with source length and radius $h = 31$ cm and $R_2 = 6.85$ cm and expansion chamber length and radius $w = 29.4$ cm and $R_1 = 15.9$ cm, the double layer potential V_s was measured as a function of the pressure p . The measurements are shown in figure 7 as the solid squares, with the theoretical curve shown as a solid line. The general shape and height of the theoretical curve match the experimental results quite well. We see experimentally the low and high pressure cutoffs for double layer formation, as also seen in the theory. At low pressures, the experimental pressure measurement is estimated to have an accuracy of about 0.1 mTorr. Figure 8 shows the theory results for the potential and the thermal ion density at 0.2 mTorr (left side), for comparison with the experimental result published in [2] (right side). The thermal ion density was measured using a retarding potential energy analyzer whose orifice was oriented at right angles to the exiting ion beam. The general shapes of the potential and the thermal ion density are quite similar to that seen experimentally. The theoretical densities agree quite well with the measurements on both sides of the double layer. A somewhat smaller double layer potential V_s

